The Ages of Passive Galaxies in a z = 1.62 Protocluster

The Astrophysical Journal, 844:43 (13pp), 2017 July 20 https://doi.org/10.3847/1538-4357/aa7948

The Ages of Passive Galaxies in a $z = 1.62$ Protocluster

Donald B. Lee-Brown[1], Gregory H. Rudnick[1], Ivelina G. Momcheva[2], Casey Papovich[3,4], Jennifer M. Lotz[2], Kim-Vy H. Tran[3,4], Brittany Henke[1], Christopher N. A. Willmer[5], Gabriel B. Brammer[2], Mark Brodwin[6], James Dunlop[7], and Duncan Farrah[8]
[1] Department of Physics and Astronomy, University of Kansas, Lawrence, KS 66047, USA; donald@ku.edu
[2] Space Telescope Science Institute, 3700 San Martin Drive, Baltimore, MD 21218, USA
[3] Department of Physics and Astronomy, Texas A&M University, College Station, TX 77843-4242 USA
[4] George P. and Cynthia Woods Mitchell Institute for Fundamental Physics and Astronomy, Texas A&M University, College Station, TX 77843-4242, USA
[5] Steward Observatory, University of Arizona, 933 N. Cherry Avenue, Tucson, AZ 85721, USA
[6] Department of Physics and Astronomy, University of Missouri, 5110 Rockhill Road, Kansas City, MO 64110, USA
[7] Institute for Astronomy, University of Edinburgh, Royal Observatory, Edinburgh, EH9 3HJ, UK
[8] Department of Physics, Virginia Tech, Blacksburg, VA 24061, USA
Received 2017 April 10; revised 2017 May 31; accepted 2017 June 11; published 2017 July 20

Abstract

We present a study of the relation between galaxy stellar age and mass for 14 members of the $z = 1.62$ protocluster IRC 0218, using multiband imaging and *HST* G102 and G141 grism spectroscopy. Using *UVJ* colors to separate galaxies into star-forming and quiescent populations, we find that, at stellar masses $M_* \geqslant 10^{10.85}\,M_\odot$, the quiescent fraction in the protocluster is $f_Q = 1.0^{+0.00}_{-0.37}$, consistent with a $\sim 2\times$ enhancement relative to the field value, $f_Q = 0.45^{+0.03}_{-0.03}$. At masses $10^{10.2}\,M_\odot \leqslant M_* \leqslant 10^{10.85}\,M_\odot$, f_Q in the cluster is $f_Q = 0.40^{+0.20}_{-0.18}$, consistent with the field value of $f_Q = 0.28^{+0.02}_{-0.02}$. Using galaxy $D_n(4000)$ values derived from the G102 spectroscopy, we find no relation between galaxy stellar age and mass. These results may reflect the impact of merger-driven mass redistribution—which is plausible, as this cluster is known to host many dry mergers. Alternately, they may imply that the trend in f_Q in IRC 0218 was imprinted over a short timescale in the protocluster's assembly history. Comparing our results with those of other high-redshift studies and studies of clusters at $z \sim 1$, we determine that our observed relation between f_Q and stellar mass only mildly evolves between $z \sim 1.6$ and $z \sim 1$, and only at stellar masses $M_* \leqslant 10^{10.85}\,M_\odot$. Both the $z \sim 1$ and $z \sim 1.6$ results are in agreement that the red sequence in dense environments was already populated at high redshift, $z \gtrsim 3$, placing constraints on the mechanism(s) responsible for quenching in dense environments at $z \geqslant 1.5$.

Key words: galaxies: clusters: individual (CLG 0218.3-0510) – galaxies: evolution – galaxies: high-redshift – galaxies: star formation

1. Introduction

In the local universe, galaxies populate two distinct regions in color–magnitude space. Red, massive galaxies, with predominantly early-type morphologies and little or no ongoing star formation, form a tight relation known as the *red sequence*, whereas the *blue cloud* consists of lower-mass, star-forming galaxies with late-type morphologies (Kauffmann et al. 2003). This bimodality is unambiguously observed to redshifts $z > 2$ (e.g., Kriek et al. 2008; Williams et al. 2009; Whitaker et al. 2013), and massive quiescent galaxies have been detected as early as $z \sim 4$ (Straatman et al. 2014).

The properties of galaxies also depend on their environment. Numerous studies have found an inverse relation between average specific star-formation rate (sSFR) and galaxy over-density, such that the average sSFR in cluster cores is much lower than that in the field, at least at low redshifts (e.g., Hashimoto et al. 1998; Lewis et al. 2002; Gómez et al. 2003; Balogh et al. 2004; Hogg et al. 2004; Patel et al. 2009; Chung et al. 2011). Additionally, by $z \sim 0$, the fraction of quiescent, lower-mass cluster galaxies relative to the field is significantly enhanced and approaches the value for the more massive central galaxies (Tal et al. 2014). These results indicate that, in addition to the intrinsic mechanisms responsible for the quenching of massive galaxies (e.g., Croton et al. 2006; Peng et al. 2010), environmentally driven processes exist; they may even play a dominant role in the quenching of lower-mass galaxies (e.g., Bassett et al. 2013; Delaye et al. 2014). A comprehensive understanding of the physical processes responsible for quiescence and their relative importance as a function of galaxy mass and environment is one of the primary objectives in extragalactic astrophysics.

Attempts to observe young clusters that are in the process of virializing have naturally pushed to higher redshifts, where massive ($M_* \geqslant 10^{10}\,M_\odot$) quiescent galaxies are building up the bulk of their stellar populations and actively shutting off their star formation. At $z \gtrsim 1$, the mix of galaxy populations is significantly different than that observed at lower redshifts, with some clusters showing evidence for high fractions of star-forming galaxies (e.g., Butcher & Oemler 1978; Tadaki et al. 2012; Brodwin et al. 2013), compared to lower-redshift clusters, recent or ongoing merging (Rudnick et al. 2012; Lotz et al. 2013), and star-forming early-type galaxies (Mei et al. 2015). Additionally, studies have argued that environmental quenching mechanisms play a secondary role in suppressing star-formation rate at these high redshifts, with intrinsic processes responsible for the bulk of the observed red sequence galaxies (e.g., Quadri et al. 2012; Brodwin et al. 2013; Fassbender et al. 2014; Nantais et al. 2016).

Still, even at $z \gtrsim 1.5$, the environment likely still plays some role in cluster red sequence assembly. In recent years, a steadily increasing number of high-redshift ($z > 1.5$) clusters or protoclusters have been discovered and confirmed (e.g., Andreon et al. 2009; Papovich et al. 2010; Gobat et al. 2011; Santos et al. 2011; Stanford et al. 2012; Zeimann et al. 2012;

Muzzin et al. 2013b; Mei et al. 2015; Webb et al. 2015; Cooke et al. 2016; Wang et al. 2016). What studies have found is that, although significant cluster-to-cluster scatter exists, $z \gtrsim 1.5$ clusters often still have well-developed red sequences and elevated quiescent fractions relative to the field (Quadri et al. 2012; Newman et al. 2014; Cooke et al. 2016; Nantais et al. 2016; but, also see Lee et al. 2015). However, it is not yet clear what mechanisms drive the observed enhanced quiescent fractions.

To address this deficiency, we focus in this work on one high-redshift dense environment, the $z = 1.62$ protocluster XMM-LSS J02182-05102 (also known as IRC 0218, and hereafter referred to as such). The protocluster was identified as an overdensity in red *Spitzer*/IRAC colors coincident with weak *XMM* X-ray emission, and subsequently spectroscopically confirmed with IMACS on the *Magellan* Telescope (Papovich et al. 2010). It was simultaneously and independently discovered and confirmed through similar methods by Tanaka et al. (2010). Various follow-up studies have accumulated a wealth of multiband photometric and spectroscopic observations (see Section 2), making the protocluster an important object for the study of high-redshift dense environments.

The mass of IRC 0218 is estimated to be around $M \sim 4$–$7 \times 10^{13}\,M_{\odot}$ (Finoguenov et al. 2010; Papovich et al. 2010; Pierre et al. 2012; Tran et al. 2015), which is lower than the most massive clusters observed at $z > 1.5$ (see, e.g., Stanford et al. 2012; Brodwin et al. 2016). Its modest mass, coupled with significant expected future accretion, make it a likely progenitor of a Virgo-mass cluster in the local universe (Hatch et al. 2016). The weakness of its intracluster X-ray emission, as observed by *Chandra,* indicates that it is not yet virialized (Pierre et al. 2012), with recent work supporting this and finding that the protocluster actually consists of several distinct subgroups in the process of assembly (Hatch et al. 2016).

The protocluster's unevolved state and low galaxy–galaxy velocity dispersion suggest a much higher merger rate than in more mature cluster environments (Papovich et al. 2010; Pierre et al. 2012; Rudnick et al. 2012; Hatch et al. 2016). Indeed, morphological studies of the red sequence population have found a lack of compact quiescent galaxies, attributed to a previous and/or currently increased merger rate in the protocluster relative to the field (Papovich et al. 2012). This explanation is supported by the direct-imaging study of Lotz et al. (2013), which found that the merger rate for the massive galaxies ($M_{*} \geqslant 10^{10}\,M_{\odot}$) is a factor of 3–10 higher than that in the field, with the bulk of the extra merging due to dry minor merging. More recently, the brightest cluster galaxy was shown to be a record-breaking gravitational lens, rather than a merger (Wong et al. 2014). However, even after adjusting for this, IRC 0218 still shows an elevated merger rate relative to the field.

Because IRC 0218 has a relatively well-developed red sequence, is still in the process of assembly, and shows evidence for elevated merger activity, it is an excellent target for investigating the buildup of the high-redshift red sequence in dense environments. In this work, we examine the relation between galaxy mass and $D_n(4000)$ (which we use as an indicator of stellar age), in order to constrain the possible explanations for the buildup of the red sequence in dense environments. For example, if mass is the primary driver of quenching at high redshifts, then there should be a clear relation between age and stellar mass. On the other hand, if, e.g., mergers have played a significant role in the buildup of the cluster's red sequence, we expect little to no relation between mass and age on the red sequence. Other environmental processes that work over a range in masses, such as strangulation (Larson et al. 1980), may also serve to flatten any $D_n(4000)$–M_{*} relation, although the low mass of the protocluster means that other possible mechanisms, such as vigorous ram pressure stripping effects (Gunn & Gott 1972), are unlikely to produce such an effect.

The outline of this work is as follows. Our data is described in Section 2. In Section 3, we explain how we selected our cluster and field samples, measured stellar masses and the $D_n(4000)$ spectroscopic index (Bruzual 1983; Balogh et al. 1999), and estimated sample completeness. In Section 4, we discuss the quiescent fraction of galaxies in the cluster and field samples, and use the measurements of $D_n(4000)$ to constrain age differences between quiescent and star-forming cluster galaxies. Finally, we discuss our results in Section 5, compare them with the results of other high-redshift galaxy cluster studies, and conclude in Section 6. Throughout, we use a ΛCDM cosmology with $\Omega_m = 0.3$, $\Omega_{\Lambda} = 0.7$, $H_0 = 70\,\mathrm{km\,s^{-1}\,Mpc^{-1}}$, and a Chabrier IMF (Chabrier 2003). Magnitudes given are in the AB system, with zero point $M_{\mathrm{AB}} = 25$.

2. Data

IRC 0218 is in the UKIDSS Ultra-Deep Survey field (UDS; Lawrence et al. 2007), and was partially imaged with the WFC3 F125W (J_{125}) and F160W (H_{160}) filters as part of the CANDELS survey (Grogin et al. 2011; Koekemoer et al. 2011). Full CANDELS-depth photometric coverage of the cluster in F125W and F160W, as well as 10 orbits of G102 grism spectroscopy of the densest protocluster subgroup, were obtained under a follow-up program (PI Papovich: GO 12590). Additionally, we use WFC3 F140W filter and G141 grism coverage of the cluster collected under the 3D-*HST* survey (Brammer et al. 2012; Momcheva et al. 2016). The photometry used for this study is contained in the v4.1.5 3D-*HST* release, and was self-consistently reduced as described in Skelton et al. (2014); both G102 and G141 data were reduced according to the procedure described in Momcheva et al. (2016).

Several example grism spectra and their accompanying SED fits are given in Figure 1. The G102 grism provides low-resolution ($R \sim 210$) spectroscopy of wavelengths $800 \leqslant \lambda \leqslant 1150$ nm, whereas the G141 grism covers $1075 \leqslant \lambda \leqslant 1700$ nm with $R \sim 130$. Thus, the grism observations cover the rest-frame 4000 Å (Balmer) break, 3727 Å [O II] region, and 4959 and 5007 Å [O III] features at the redshift of the protocluster. The range of spectroscopic coverage provided by the two grisms, along with the extensive photometric data, enables precise redshift determinations through SED fitting. In Figure 2, we show the redshift probability distributions for the three galaxies given in Figure 1. The probability distributions derived from the jointly fit grism and photometric data are significantly better constrained than the distributions from photometry alone. This is largely due to resolution of fine spectral features in the grism data, and illustrates the utility of *HST* grism data in determining galaxy redshifts at early epochs.

As a final note, some of the galaxies in IRC 0218 have redshifts derived from higher-resolution ground-based spectroscopy (Subaru/MOIRCS: Tanaka et al. 2010, *Magellan*/IMACS: Papovich et al. 2010, KECK/MOSFIRE+LRIS: Tran

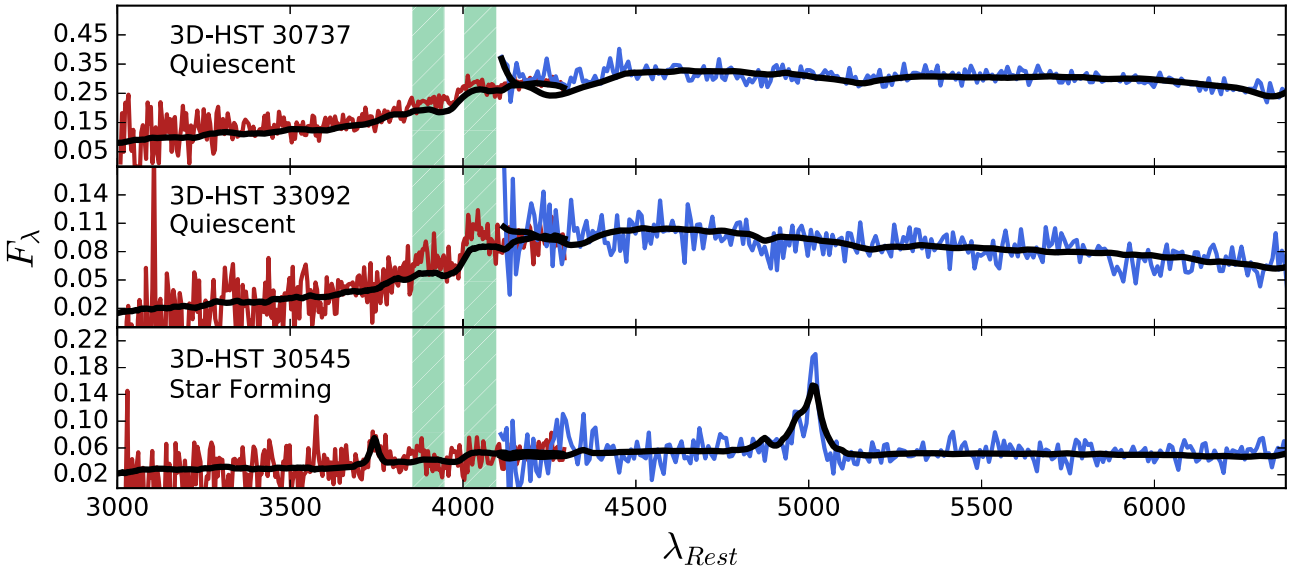

Figure 1. Rest-frame G102 (red) and G141 (blue) grism spectra of three galaxies in IRC 0218, plotted from ∼3000 to 6850 Å. The colored lines are measured fluxes, and the black lines are best-fit SED models. The two grism spectra for each galaxy were fit independently, resulting in some model discontinuity where the grism wavelength ranges overlap, ∼4200 Å. The vertical striped bars denote the upper and lower $D_n(4000)$ indices (see Section 3.2). Galaxy classifications (quiescent or star-forming) are described in Section 4.1.

et al. 2015). In general, preference was given to these redshifts—except in three cases where the grism-based redshifts were indisputably superior. Nearly all of these ground-based redshifts (except a few from Tanaka et al. (2010)) were obtained from emission lines. Significantly deeper continuum spectroscopy is needed to obtain quiescent galaxy redshifts. With the grism, we are able to measure precise 4000 Å-based redshifts of quiescent galaxies. The procedure by which the grism redshifts were derived is detailed in Section 3.2.

3. Sample Selection and Completeness

3.1. The Field and Protocluster Grism Samples

We select our spectroscopic field and protocluster samples from the galaxies with G102 coverage of the rest-frame 4000 Å break, which limits our samples to galaxies in the redshift range $1.27 \lesssim z \lesssim 1.77$. Additionally, the spatial extent of the spectroscopic samples is limited to the single 3D-*HST* field UDS-18, the only field for which we have the requisite G102 coverage. Comparison of the SED fit-derived grism+photometric redshifts with those obtained by higher-resolution ground-based spectroscopy indicates an average deviation of $\overline{\Delta z} = 0.01$ at the protocluster redshift, so we construct the cluster sample using all 25 galaxies with redshifts $z = 1.62 \pm 0.02$ in the field. Our field grism sample contains 38 galaxies with redshifts $1.27 \leqslant z \leqslant 1.58$, $1.66 \leqslant z \leqslant 1.77$, although we also make use of a much larger field sample composed of photometric sources (detailed in Section 4.1).

3.2. Measurement of Stellar Masses and $D_n(4000)$

Stellar masses for the protocluster and field galaxies were estimated through template fits to the rest-frame photometry, using the fitting code FAST (Kriek et al. 2009). For the template fits, we adopted the maximally likely redshifts from the redshift probability distributions derived from available G141, G102, and photometric data. As a galaxy's redshift probability distribution is, in general, non-Gaussian, upper and lower 68% redshift confidence intervals were estimated through resampling. The protocluster sample contains 10 galaxies with precision redshifts measured from high-resolution spectroscopy; for these galaxies, we fix their redshifts to the spectroscopic values. Bruzual & Charlot (2003) stellar population models were used to generate templates with ages in the range of $10^{7.6} \leqslant t/\mathrm{year} \leqslant 10^{10.1}$, and exponentially declining star-formation histories with τ in the range of $10^7 \leqslant \tau/\mathrm{year} \leqslant 10^{10}$ year. Metallicity was fixed at $Z = 0.02$, to be consistent with the 3D-*HST* catalogs and avoid the large uncertainties associated with modeling galaxy chemical evolution. The dust law of Calzetti et al. (2000) was adopted for the template fitting, although we note that galaxy mass is relatively insensitive to the specific choice of dust law.

The rest-frame 4000 Å break is due to line blanketing—primarily Ca and Fe lines—of the stellar continuum emission from lower-mass (F, G, and K spectral type) dwarfs and giants. Young stellar populations will have weak 4000 Å breaks due to the luminosity contribution from high-mass stars, whereas old populations with prominent absorption lines will have the strongest 4000 Å breaks. Thus, the $D(4000)$ spectroscopic index (Bruzual 1983), defined to be the ratio of flux above the 4000 Å break to the flux below it, provides a straightforward estimate of a galaxy's luminosity-weighted age (see, e.g., Rudnick et al. 2000; Kauffmann et al. 2003). In this work, we adopt the wavelength definitions of Balogh et al. (1999), i.e., the index is defined to be the ratio of mean rest-frame flux in the region $4000 \leqslant \lambda \leqslant 4100$ Å to the flux in the region $3850 \leqslant \lambda \leqslant 3950$ Å; we denote this as $D_n(4000)$. The principal advantage of $D_n(4000)$ over the original index definition of Bruzual (1983) is its insensitivity to reddening effects, which we confirmed with extensive simulations. We note that measurements of $D_n(4000)$ from simulated spectra degraded to the G102 grism resolution show no systematic offsets, relative to measurements at higher resolutions (Henke 2015).

The method used to estimate the uncertainties in $D_n(4000)$ is as follows. First, one-dimensional, optimally weighted spectra were extracted from the 2D G102 grism spectra, following the

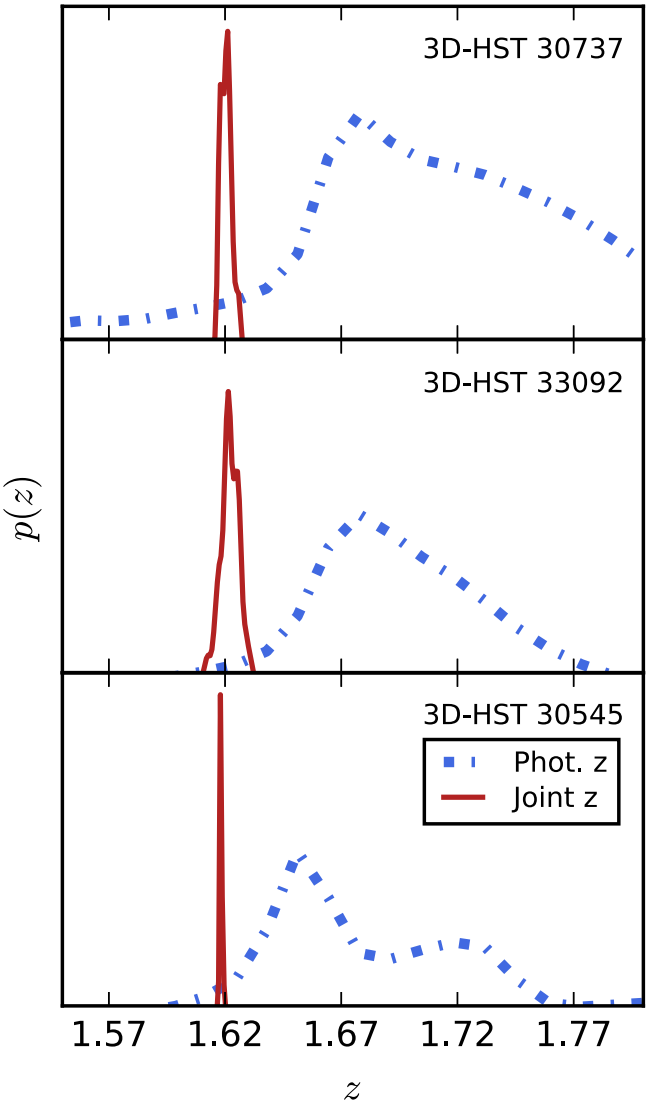

Figure 2. Redshift probability distributions for the three galaxies shown in Figure 1. The solid red line indicates the $p(z)$ derived from jointly fitting the G102, G141, and photometric data. The dashed blue line shows the $p(z)$ derived from fitting the photometric data alone. For visualization purposes, the probability distributions for each galaxy are scaled by a multiplicative factor relative to one another.

method of Horne (1986). Next, a redshift was randomly drawn from the per-galaxy redshift probability grid derived from jointly fitting the G102, G141, and photometric data. For the joint-fit redshifts, typical redshift probability grid step sizes are $\Delta z \lesssim 10^{-3}$; we nonetheless linearly interpolated onto a 10x denser grid before the random draw. If a galaxy had a high-quality, ground-based spectroscopic redshift, this redshift was selected instead and fixed. Finally, under the assumption of normally distributed flux uncertainties, the flux in each wavelength bin was randomly drawn, and an appropriately redshifted $D_n(4000)$ calculated. Linear interpolation was used to estimate the flux in partial wavelength bins at the index boundaries. After 100,000 iterations of this process for each galaxy, upper and lower 68% confidence intervals were calculated for each measured $D_n(4000)$. These uncertainties are based on redshift and flux uncertainties alone; we assess the metallicity dependence of $D_n(4000)$ in Section 5.

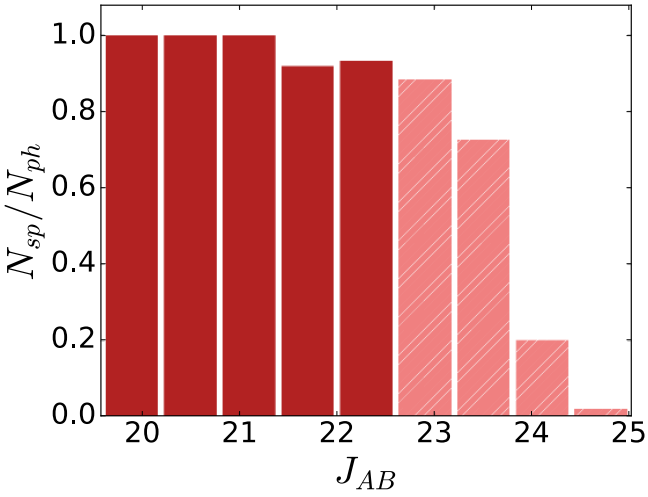

Figure 3. G102 completeness, given as the ratio of spectroscopic to photometric detections, as a function of 3D-*HST* $J_{\rm AB}$ magnitude. Solid bars indicate galaxies above our 90% spectroscopic completeness limit, which occurs at $J_{\rm AB} = 22.6$.

3.3. Completeness

We estimated the spectroscopic and mass completeness of our sample by comparing the G102 sample with the much deeper photometric catalog in the spatial region of the protocluster. We find that 90% of the photometric sources with $J_{\rm AB} \leqslant 22.6$ have extracted grism spectra (Figure 3). This limiting magnitude was then used to obtain an empirical estimate of the spectroscopic mass completeness, following the procedure of Marchesini et al. (2009). To do this, we selected *photometric* sources with $22.0 \leqslant J_{\rm AB} \leqslant 23.0$ and redshifts $1.40 \leqslant z \leqslant 1.75$, then scaled their $J_{\rm AB}$ luminosities to the $J_{\rm AB} \leqslant 22.6$ spectroscopic limit, holding the galaxy mass-to-light ratio (M/L) constant. Under the assumption that the distribution of galaxy M/L is unchanged over the magnitude and redshift ranges we used, the luminosity scaling process creates a simulated, relatively complete population at the spectroscopic limit. The high-mass end of the simulated population then gives an estimate of the mass completeness. We find our 95% grism mass-completeness limit to be $10^{10.2}\,M_{\odot}$; moderate changes to this limit ($10^{10.2\pm0.1}\,M_{\odot}$) do not impact the results of this study. In the protocluster, $14/25$ extracted grism sources are above the mass completeness limit; in the field, $12/38$ sources are above the cutoff.

4. Results

4.1. The Quiescent Fraction in IRC 0218 and the Field

The protocluster and field samples were separated into quiescent and star-forming populations, according to their positions in the $(U-V)$, $(V-J)$ rest-frame color plane. Separating galaxies in the *UVJ* plane allows for a distinction between quiescent galaxies and dust-obscured, star-forming galaxies that might appear quiescent based on their $(U-V)$ colors alone (see Wuyts et al. 2007; Williams et al. 2009). Here, we follow the criteria established by Whitaker et al. (2012) and used in Whitaker et al. (2013), and define galaxies to be quiescent if they are contained in the region $(U-V) > 0.8 \times (V-J) + 0.7$, $(U-V) > 1.3$, $(V-J) < 1.5$. The results of this selection process are given in Figure 4. Several galaxies in the field and cluster are quite close to the selection

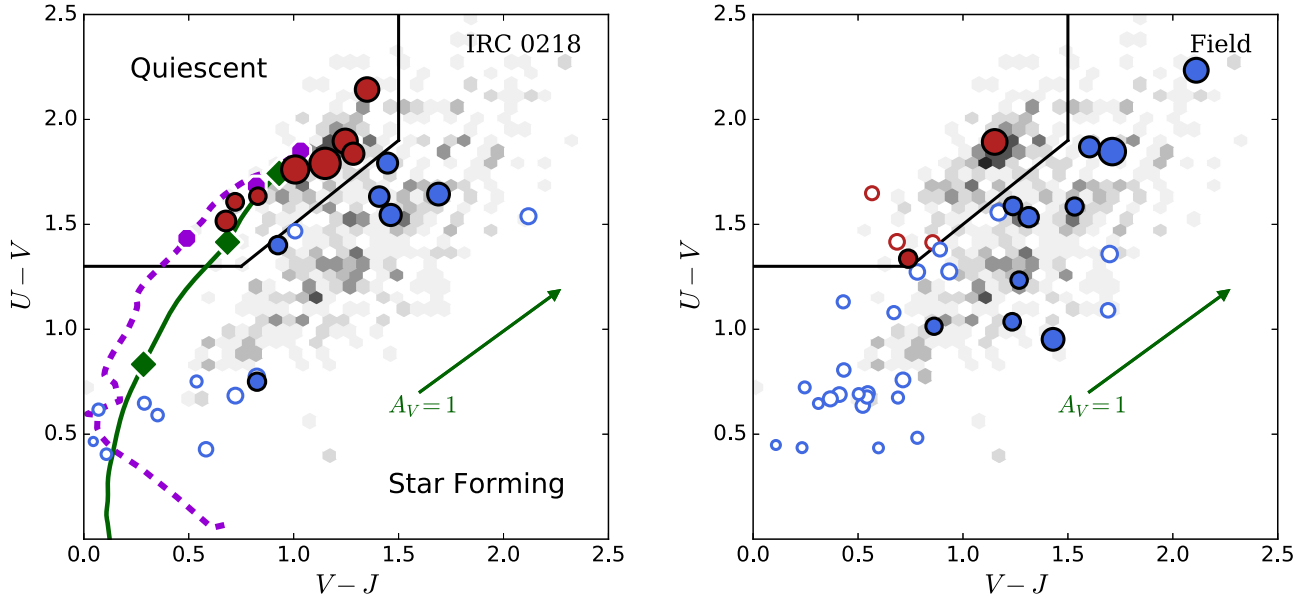

Figure 4. $(U - V)$, $(V - J)$ color–color diagrams for the protocluster and field samples. Points in the upper left bounded region of each plot are classified as quiescent, whereas points outside the region are classified as star-forming. Point size indicates mass, logarithmically scaled relative to the most massive quiescent protocluster galaxy, $M_* = 10^{11.48}\,M_\odot$. Open points represent galaxies below the adopted mass completeness threshold of $M_* = 10^{10.2}\,M_\odot$. The grayscale region shows the colors of the full 3D-*HST* G141 grism sample above the mass completeness threshold in the redshift range $1 \leqslant z \leqslant 2$. In the left panel, the dashed line traces the rest-frame color evolution for a $Z = 0.02$ single stellar population from 10 Myr to 2.2 Gyr, as predicted by Bruzual & Charlot (2003) SED models. The solid line traces evolution over the same period of time for a population with an exponential SFH with $\tau = 300$ Myr. Successive points on the evolution tracks (from left to right) indicate the predicted $z = 1.62$ colors for populations with $z_f = 2.0$, 2.5, and 3.5. The arrows indicate the change in $(U - V)$ and $(V - J)$ expected for a one magnitude increase in reddening in V, following a Calzetti et al. (2000) extinction law.

boundary. At the end of this section, we discuss the sensitivity of our results to the specific adopted *UVJ* cuts.

We find that, above our mass completeness limit, 8/14 protoclusters and 2/12 field galaxies meet our adopted requirements for quiescence. Defining the quiescent fraction as $f_Q = n_Q/(n_{\rm SF} + n_Q)$, where n_Q and $n_{\rm SF}$ are the numbers of quiescent and star-forming galaxies, respectively, we find that $f_Q = 0.57^{+0.15}_{-0.17}$ in the protocluster, and $f_Q = 0.17^{+0.18}_{-0.11}$ in the field. The upper and lower uncertainties given are the 68% binomial confidence intervals, calculated according to Gehrels (1986).

As our definition of quiescence only uses *UVJ* information, and our stellar mass values are derived from photometry, we extended the field sample to include all sources from the five 3HDST fields (UDS, GOODS-N, GOODS-S, COSMOS, and AEGIS), in order to avoid the larger uncertainties due to the small size of the G102 field sample. This extended field sample has 1151 galaxies with masses $M_* \geqslant 10^{10.2}\,M_\odot$ over the redshift range $1.52 \leqslant z \leqslant 1.76$, after exclusion of known IRC 0218 galaxies. Of these galaxies, 366 are quiescent and 785 are star-forming, according to their *UVJ* plane positions. From this sample, we obtain $f_Q = 0.32^{+0.01}_{-0.01}$; consistent with the G102 field sample, but considerably more precise. Thus, we conclude that, considering all galaxies with $M_* \geqslant 10^{10.2}\,M_\odot$, the protocluster is approximately twice as quenched as the field.

More interesting is examining how f_Q varies as a function of stellar mass for the field and protocluster. For the protocluster sample, we calculated mean f_Q in two mass bins, where the boundary between the bins was taken to be the midpoint of the range in mass spanned by the most massive protocluster galaxy and the mass completeness limit, $M_{\rm split} = 10^{10.85}\,M_\odot$. For the field, galaxies were separated into six mass bins spanning $10^{10.2} \leqslant M_* \leqslant 10^{11.5}$. The results of this process are given in Table 1 and shown in Figure 5. We also calculated the cluster conversion fraction, or efficiency of quenching due to environment, according to the relation $f_C = (f_{Q,\rm cluster} - f_{Q,\rm field})/(1 - f_{Q,\rm field})$ (van den Bosch et al. 2008; Phillips et al. 2014; Balogh et al. 2016; Nantais et al. 2017). We give these values in Table 1 to facilitate comparison with other cluster studies, but leave interpretation of our values for future work.

We find evidence suggesting that the values of f_Q in the cluster and field diverge at high masses. At low masses, $10^{10.2}\,M_\odot \leqslant M_* \leqslant 10^{10.85}\,M_\odot$, we find $f_Q = 0.40^{+0.18}_{-0.20}$ for the protocluster sample. This value is consistent with the field sample over the same mass range, where we find $f_Q = 0.28^{+0.02}_{-0.02}$. At higher masses, however, $10^{10.85}\,M_\odot \leqslant M_* \lesssim 10^{11.5}\,M_\odot$, $f_Q = 1.00^{+0.00}_{-0.37}$ in the protocluster; the field value is $f_Q = 0.45^{+0.03}_{-0.03}$. Thus, under the specific adopted binning scheme, the protocluster f_Q is marginally consistent with enhancement above the field value at high masses.

With regards to the stability of this result, we are hampered by the small protocluster galaxy sample size and correspondingly large binomial uncertainties. In both the high- and low-mass cluster bins, the median galaxy mass is similar to (within $\sim$0.1 dex of) the value for the respective field bin, so we do not believe our results are biased by differences in the galaxy mass function between the protocluster and field. However, our results are relatively sensitive to the adopted binning scheme used for calculating f_Q. For example, if we adopt bins that encompass equal numbers of protocluster galaxies, rather than bins encompassing equal ranges in mass, then at high masses the protocluster and field f_Q values are within 1σ of one another. Thus, we avoid placing strong emphasis on the f_Q results from our protocluster alone, and instead interpret our results in light of other high-redshift dense environments (see Section 5).

Table 1
Mass, f_Q, and f_C

$\log(M/M_\odot)$	N_Q	N_{SF}	f_Q	f_C
		IRC 0218		
11.175	4	0	$1.00^{+0.00}_{-0.37}$	$1.00^{+0.00}_{-0.63}$
10.525	4	6	$0.40^{+0.20}_{-0.18}$	$0.33^{+0.23}_{-0.23}$
		Field (coarse mass bins)		
11.175	108	132	$0.45^{+0.03}_{-0.03}$	⋯
10.525	258	653	$0.28^{+0.02}_{-0.02}$	⋯
		Field (fine mass bins)		
11.3	23	30	$0.43^{+0.08}_{-0.08}$	⋯
11.1	35	47	$0.43^{+0.06}_{-0.06}$	⋯
10.9	67	78	$0.46^{+0.04}_{-0.04}$	⋯
10.7	101	153	$0.40^{+0.03}_{-0.03}$	⋯
10.5	84	206	$0.29^{+0.03}_{-0.03}$	⋯
10.3	56	271	$0.17^{+0.02}_{-0.02}$	⋯

Note. Only the mass-complete protocluster sample considered here. The field sample is drawn from all five 3D-*HST* fields. Masses correspond to bin centers; bin widths are $\Delta\log(M/M_\odot) = 0.65$ for the protocluster and coarsely binned field sample and $\Delta\log(M/M_\odot) = 0.20$ for the field sample with finer mass binning. In order for the fine bins to encompass the same mass range as the coarse binning scheme, the bin at $\log(M/M_\odot) = 11.3$ extends to $\log(M/M_\odot) = 11.5$. The conversion fraction f_C is calculated relative to the larger 3D-*HST* field sample.

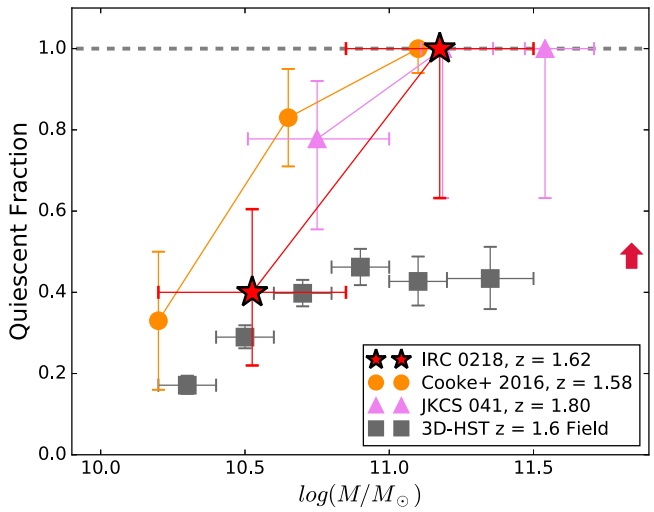

Figure 5. The quiescent fraction of galaxies as a function of stellar mass from this work (red stars). We also give the quiescent fractions from the Newman et al. (2014) study of the $z = 1.80$ cluster JKCS 041 (pink triangles) and the work by Cooke et al. (2016) on a $z = 1.58$ cluster near the radio galaxy 7C 1753 + 6311 (orange circles) (see Section 5). The field sample (gray squares) is composed of all galaxies in the full 3D-*HST* G141 grism sample with redshifts $1.52 \leqslant z \leqslant 1.76$, excluding known IRC 0218 galaxies. The arrow on the right side of the plot indicates the approximate change in f_Q if quiescent galaxies were selected according to the *UVJ* criteria of Williams et al. (2009).

We also note that the exact value of f_Q depends on the *UVJ* criteria that are adopted. For example, if we adopt the slightly different Williams et al. (2009) *UVJ* criteria, three star-forming galaxies above our mass limit—two in the protocluster and one in the field—would be reclassified as quiescent. Under such a change, we would find $f_Q = 0.60^{+0.18}_{-0.21}$ and $f_Q = 0.32^{+0.02}_{-0.02}$ for the low-mass protocluster and field bins, respectively. At high masses, under the Williams et al. (2009) criteria, we would find $f_Q = 1.00^{+0.00}_{-0.37}$ and $f_Q = 0.52^{+0.03}_{-0.03}$ in the protocluster and field, respectively. Therefore, our conclusions regarding the behavior of f_Q at high masses are stable against moderate changes in *UVJ* criteria, but at lower masses some caution must be exercised, due to possible *UVJ* selection effects. In Tables 2 and 3, we provide individual galaxy *UVJ* measurements, along with the other parameters used in this study, for the cluster and field grism samples, respectively.

4.2. $D_n(4000)$ and Stellar Mass

We now turn our attention to $D_n(4000)$ and its ability to constrain age differences between galaxies in IRC 0218. In Figure 6, we show $D_n(4000)$ as a function of stellar mass for the protocluster and field G102+G141 samples. The process by which $D_n(4000)$ was measured is detailed in Section 3.2. Here, our mass-complete field sample consists of the 12 galaxies in the spatial region covered by the G102 grism, with redshifts $1.27 \leqslant z \leqslant 1.58$, $1.66 \leqslant z \leqslant 1.77$. The cluster sample is the same as in Section 4.1.

We first compare the mean $D_n(4000)$ values for quiescent and star-forming protocluster galaxies with mean values for field galaxies. We find that the weighted mean $D_n(4000)$ for quiescent galaxies in the protocluster is $\mu_Q = 1.39 \pm 0.03$, where the weight associated with each $D_n(4000)$ value is taken as the estimate of inverse variance derived from the measure's 68% confidence interval. For the star-forming galaxies in the cluster, $\mu_{SF} = 1.22 \pm 0.06$. In the field, we find that $\mu_Q = 1.41 \pm 0.03$; this is consistent with the cluster value, albeit we note that our field sample only contains two quiescent galaxies. However, $\mu_{SF} = 0.94 \pm 0.04$ in the field, driven by a galaxy with a very low, well-constrained $D_n(4000)$ value. Because we report weighted mean $D_n(4000)$ values here, this measurement dominates the reported μ_{SF}. Removing it from the calculation results in $\mu_{SF} = 1.20 \pm 0.08$ in the field.

Such a dramatic change indicates that more field galaxies with accurate $D_n(4000)$ measurements are needed before drawing any conclusions regarding any differences between the star-forming field and protocluster populations. Likewise, differences in the scatter of $D_n(4000)$ measurements in the different environments could potentially yield important information as to the relative star-formation histories (SFHs) of cluster and field galaxies. However, the small numbers of galaxies in our samples preclude the precise measurement of the scatter. Future larger samples of $D_n(4000)$ will be needed to do this.

Using the same mass bins as in Section 4.1, and now considering all protocluster galaxies (both quiescent and star-forming), we find the weighted mean $D_n(4000)$ at stellar masses $10^{10.85}\,M_\odot \leqslant M_* \lesssim 10^{11.5}\,M_\odot$ to be $\mu_{high} = 1.38 \pm 0.03$. For masses $10^{10.2}\,M_\odot \leqslant M_* \leqslant 10^{10.85}\,M_\odot$, we find $\mu_{low} = 1.31 \pm 0.05$. Thus, there is little difference in mean $D_n(4000)$ between the two mass ranges. This result is unchanged under changes to the mass-binning scheme. For example, adopting the equal-number binning discussed in Section 4.1 would result in closer agreement between the high- and low-mass subsamples.

The $D_n(4000)$ values we calculate for IRC 0218 galaxies are generally much lower than those observed in the local universe. In Figure 6, we show the approximate locus of $D_n(4000)$ values from an analysis of Sloan Digital Sky Survey (SDSS) galaxies by Kauffmann et al. (2003). At high masses, the mean $D_n(4000)$ value in the protocluster corresponds to the lowest few percent of $D_n(4000)$ values for the entire SDSS sample. At

Table 2
IRC 0218 Galaxy Sample

3D-*HST* ID	Q/SF	z	$J_{\mathrm{AB_{rest}}}$	$(U-V)_{\mathrm{rest}}$	$(V-J)_{\mathrm{rest}}$	$\log(M/M_{\odot})$	$D_n(4000)$
31684	Q	$1.631^{+0.003}_{-0.008}$	19.82	1.79	1.15	11.48	$1.56^{+0.08}_{-0.08}$
30737	Q	1.621[a,b]	19.60	1.76	1.01	11.26	$1.35^{+0.03}_{-0.03}$
36010	Q	$1.628^{+0.003}_{-0.003}$	20.39	1.90	1.25	11.03	$1.32^{+0.13}_{-0.10}$
29983	Q	$1.629^{+0.003}_{-0.003}$	20.52	2.14	1.35	10.97	$1.54^{+0.12}_{-0.13}$
30169	SF	1.629[b]	20.67	1.64	1.69	10.82	$1.16^{+0.32}_{-0.23}$
29899	Q	$1.620^{+0.005}_{-0.006}$	20.98	1.84	1.28	10.77	$2.23^{+0.34}_{-0.29}$
30545	SF	1.624[a,b]	20.71	1.54	1.46	10.76	$1.15^{+0.12}_{-0.12}$
29007	SF	$1.624^{+0.004}_{-0.005}$	20.84	1.79	1.45	10.65	$1.43^{+0.13}_{-0.14}$
33092	Q	$1.621^{+0.004}_{-0.004}$	21.19	1.52	0.68	10.62	$1.49^{+0.09}_{-0.09}$
32696	SF	$1.625^{+0.006}_{-0.082}$	21.03	1.63	1.41	10.60	$1.43^{+0.29}_{-0.18}$
31086	SF	1.623[b]	21.75	1.40	0.92	10.38	$1.22^{+0.16}_{-0.15}$
31703	SF	1.623[b,c]	21.71	0.75	0.83	10.36	$1.14^{+0.11}_{-0.09}$
28015	Q	$1.620^{+0.001}_{-0.001}$	21.94	1.61	0.72	10.30	$0.95^{+0.44}_{-0.32}$
27956	Q	$1.629^{+0.063}_{-0.214}$	22.17	1.63	0.83	10.27	$1.37^{+0.69}_{-0.42}$
			Mass Incomplete				
31715	SF	$1.626^{+0.004}_{-0.002}$	22.24	0.77	0.82	10.15	$1.23^{+0.25}_{-0.20}$
30456	SF	$1.610^{+0.028}_{-0.004}$	21.55	1.54	2.12	10.08	$1.48^{+1.90}_{-0.89}$
30472	SF	1.623[b]	22.21	0.68	0.72	10.05	$1.12^{+0.09}_{-0.10}$
35210	Q	$1.632^{+0.013}_{-0.220}$	23.11	1.47	1.01	9.87	$1.17^{+1.36}_{-0.62}$
29841	SF	$1.623^{+0.001}_{-0.001}$	22.60	0.43	0.58	9.86	$0.91^{+0.10}_{-0.08}$
33093	SF	1.629[b,c]	23.06	0.65	0.29	9.63	$1.36^{+0.32}_{-0.27}$
32608	SF	1.626[b]	23.19	0.59	0.35	9.55	$0.96^{+0.18}_{-0.17}$
28036	SF	$1.619^{+0.003}_{-0.003}$	23.24	0.62	0.07	9.51	$1.30^{+0.35}_{-0.26}$
29050	SF	1.624[b]	23.38	0.75	0.54	9.48	$0.62^{+0.16}_{-0.13}$
33068	SF	1.624[b]	23.60	0.40	0.11	9.38	$1.12^{+0.35}_{-0.32}$
30952	SF	$1.629^{+0.001}_{-0.004}$	24.41	0.47	0.05	8.88	$0.79^{+0.34}_{-0.23}$

Notes. Redshifts with no reported uncertainty are spectroscopic, and are averages if multiple measurements exist.
[a] Tanaka et al. (2010).
[b] Tran et al. (2015).
[c] Papovich et al. (2010).

lower masses, the mean protocluster value is still lower than for the SDSS galaxies. These results indicate that, as expected, the galaxies we observe at $z = 1.6$ contain much younger stellar populations than at $z \sim 0$. We discuss the implications of these results (under certain assumptions) in Section 5.

A primary goal of this study was to place constraints on any relation between red sequence galaxy age and mass; we therefore used weighted linear regression to fit the red sequence $D_n(4000)$ values as a function of stellar mass for protocluster galaxies. Weights were again chosen to be the estimate of inverse variance derived from the average 68% confidence interval for each galaxy. Uncertainties on the fit were determined by bootstrapping. The results of our regression analysis are given in Figure 6. Within the 68% uncertainties associated with our fit, we are consistent with slopes ranging from $\Delta D_n(4000) = +0.25$ log $(M_{\odot})^{-1}$ to $\Delta D_n(4000) = -0.2$ log $(M_{\odot})^{-1}$ over our mass interval.

Thus, we cannot reject the null hypothesis that there is no relation between $D_n(4000)$ and stellar mass for quiescent galaxies above our mass completeness limit. Depending on adopted SFH, $D_n(4000)$ can begin to saturate as early as $D_n(4000) \sim 1.6$ for solar-metallicity models, losing its ability to differentiate between galaxies of different age. This saturation threshold is somewhat lower for lower metallicities. However, few of the protocluster galaxies have $D_n(4000)$ values close to this level; we can therefore rule out saturation as the underlying cause for a flat relation, unless the galaxies we observe have $Z < Z_{\odot}/5$. This is unlikely, given the relatively high stellar mass range posed here, and based on the metallicity of star-forming galaxies in this same protocluster (Tran et al. 2015). The implications of a flat relation for the stellar age distribution of the protocluster galaxies under certain model assumptions are discussed further in Section 5.

Our $D_n(4000)$ results are robust against moderate changes to the underlying *UVJ* quiescent/star-forming classifications. Under the reclassification of the three galaxies discussed at the end of Section 4.1, the significance of the difference between star-forming and quiescent galaxies in IRC 0218 would be essentially unchanged: $\mu_Q = 1.39 \pm 0.03$ and $\mu_{\mathrm{SF}} = 1.17 \pm 0.07$. Additionally, under such a reclassification, we still cannot reject the null hypothesis of no relation between $D_n(4000)$ and galaxy mass for quiescent protocluster galaxies.

5. Discussion

5.1. The Quiescent Fraction in IRC 0218

As discussed in Section 4.1 and shown in Figure 5, in IRC 0218, the quiescent fraction at $M_* \geqslant 10^{10.85}\,M_{\odot}$ is consistent with being two times higher than in the field. Although the strength of this conclusion is hampered by a small sample size, it is similar to the results from clusters at similar mass and redshift (Newman et al. 2014; Cooke et al. 2016). Considering

Table 3
Field Galaxy Sample

3D-*HST* ID	Q/SF	z	$J_{\mathrm{AB}_{\mathrm{rest}}}$	$(U-V)_{\mathrm{rest}}$	$(V-J)_{\mathrm{rest}}$	$\log(M/M_{\odot})$	$D_n(4000)$
29179	SF	$1.562^{+0.007}_{-0.010}$	20.25	1.85	1.71	11.21	$2.48^{+2.00}_{-0.86}$
32904	Q	$1.322^{+0.001}_{-0.001}$	19.69	1.89	1.15	11.07	$1.42^{+0.03}_{-0.03}$
32468	SF	$1.308^{+0.018}_{-0.030}$	20.45	2.23	2.11	11.00	$-0.12^{+0.51}_{-0.61}$
34899	SF	$1.289^{+0.001}_{-0.001}$	21.03	0.95	1.43	10.82	$0.87^{+0.05}_{-0.04}$
33670	SF	$1.416^{+0.034}_{-0.005}$	20.88	1.87	1.60	10.65	$2.21^{+3.79}_{-2.57}$
32166	SF	$1.324^{+0.004}_{-0.003}$	20.79	1.53	1.31	10.58	$1.02^{+0.15}_{-0.13}$
33472	SF	$1.330^{+0.006}_{-0.007}$	21.24	1.59	1.24	10.39	$1.59^{+0.23}_{-0.21}$
28822	Q	$1.756^{+0.002}_{-0.002}$	21.66	1.34	0.74	10.37	$1.32^{+0.09}_{-0.10}$
33524	SF	$1.606^{+0.010}_{-0.233}$	22.21	1.58	1.53	10.35	$1.40^{+0.92}_{-0.55}$
30994	SF	$1.278^{+0.001}_{-0.002}$	21.55	1.04	1.23	10.28	$1.13^{+0.11}_{-0.18}$
34916	SF	$1.539^{+0.027}_{-0.029}$	21.93	1.23	1.27	10.26	$1.51^{+0.25}_{-0.34}$
27657	SF	$1.452^{+0.007}_{-0.008}$	21.86	1.01	0.86	10.24	$1.48^{+0.27}_{-0.19}$
				Mass Incomplete			
28211	SF	$1.531^{+0.015}_{-0.014}$	22.06	1.36	1.70	10.14	$16.78^{+36.52}_{-17.56}$
29879	Q	$1.670^{+0.004}_{-0.135}$	22.39	1.56	1.17	10.12	$1.82^{+1.63}_{-0.91}$
35978	SF	$1.726^{+0.238}_{-0.088}$	23.10	1.28	0.93	10.08	$1.76^{+3.50}_{-1.74}$
32931	Q	$1.565^{+0.004}_{-0.003}$	22.47	1.42	0.69	10.03	$1.11^{+0.25}_{-0.16}$
31745	SF	$1.507^{+0.189}_{-0.050}$	22.35	1.27	0.78	10.01	$1.56^{+1.37}_{-0.68}$
31128	SF	$1.553^{+0.001}_{-0.001}$	22.21	0.67	0.37	9.95	$0.94^{+0.10}_{-0.07}$
31079	SF	$1.393^{+0.001}_{-0.001}$	21.87	0.76	0.71	9.91	$1.11^{+0.08}_{-0.08}$
36949	SF	$1.665^{+0.005}_{-0.092}$	22.50	0.69	0.41	9.90	$1.29^{+0.22}_{-0.12}$
35083	Q	$1.729^{+0.038}_{-0.028}$	23.09	1.41	0.86	9.89	$1.17^{+0.96}_{-0.35}$
27454	SF	$1.409^{+0.001}_{-0.001}$	21.62	1.09	1.69	9.87	$0.47^{+0.17}_{-0.16}$
33889	SF	$1.539^{+0.003}_{-0.005}$	22.46	0.64	0.52	9.85	$1.05^{+0.11}_{-0.10}$
28584	SF	$1.290^{+0.001}_{-0.007}$	22.36	0.70	0.55	9.80	$1.48^{+0.22}_{-0.25}$
34940	Q	$1.460^{+0.057}_{-0.022}$	22.91	1.38	0.89	9.80	$1.32^{+0.49}_{-0.48}$
31176	Q	$1.554^{+0.002}_{-0.001}$	23.36	1.65	0.57	9.79	$1.94^{+2.31}_{-0.93}$
37588	SF	$1.755^{+0.002}_{-0.002}$	23.10	0.81	0.43	9.71	$1.12^{+0.29}_{-0.23}$
27068	SF	$1.499^{+0.002}_{-0.001}$	22.46	0.68	0.54	9.68	$1.26^{+0.24}_{-0.19}$
33615	SF	$1.719^{+0.028}_{-0.047}$	23.28	1.13	0.43	9.66	$1.56^{+0.60}_{-0.61}$
31068	SF	$1.718^{+0.004}_{-0.040}$	23.60	1.08	0.67	9.66	$0.67^{+0.52}_{-0.31}$
27102	SF	$1.518^{+0.001}_{-0.001}$	22.98	0.48	0.78	9.48	$1.56^{+0.42}_{-0.34}$
35385	SF	$1.316^{+0.009}_{-0.070}$	23.01	0.67	0.69	9.48	$0.93^{+0.36}_{-0.16}$
34110	SF	$1.410^{+0.002}_{-0.002}$	23.27	0.69	0.50	9.46	$1.20^{+0.18}_{-0.17}$
28706	SF	$1.484^{+0.105}_{-0.012}$	23.38	0.72	0.25	9.45	$4.57^{+5.21}_{-3.61}$
33427	SF	$1.726^{+0.001}_{-0.003}$	23.90	0.44	0.23	9.26	$6.81^{+13.82}_{-10.25}$
36977	SF	$1.291^{+0.001}_{-0.002}$	23.41	0.65	0.31	9.25	$0.72^{+0.15}_{-0.14}$
32732	SF	$1.695^{+0.001}_{-0.007}$	23.58	0.43	0.60	9.24	$1.84^{+0.51}_{-0.44}$
28114	SF	$1.479^{+0.005}_{-0.003}$	24.32	0.45	0.11	9.05	$1.28^{+1.25}_{-0.68}$

these three dense environments together, the implication is that, even at such high redshifts of these clusters, the environment has already played some role in populating the red sequence.

Comparing these results to those of Nantais et al. (2016), which we do not show in Figure 5 due to differences in *UVJ* selection criteria, we find that the quiescent fractions plotted in Figure 5 are systematically higher at high masses by $\Delta f_Q \sim 0.2$–0.3. It is not immediately clear what may be driving this discrepancy. As noted, the *UVJ* selection criteria for quiescence are slightly different in Nantais et al. (2016), but adopting their criteria actually worsens the discrepancy—the cluster quiescent fractions remain relatively unchanged because most galaxies are well-separated from the selection boundary, but the field fraction actually decreases on average.

Alternately, the discrepancy may just be a reflection of large cluster-to-cluster variance at high redshift. Both Nantais et al. (2016) and Hatch et al. (2016) note that environmental quenching efficiency may depend on the time galaxies have spent in the cluster environment, and several studies have found that star-formation activity varies appreciably even among similarly selected clusters Brodwin et al. (2013), Alberts et al. (2016). Because the main group in IRC 0218 (which we examine in this work) appears to be more evolved, on average, than similar-redshift protoclusters (Hatch et al. 2016), and JKCS 041 has a very well-developed red sequence for its redshift Newman et al. (2014), the discrepancies in the high-mass quiescent fraction may be driven by the specific assembly histories of the clusters being compared. That is, the high-redshift environments we show in Figure 5 may be more evolved than the Nantais et al. (2016) clusters. Indeed, it may be that clusters selected by different methods have systematically different quenched fractions.

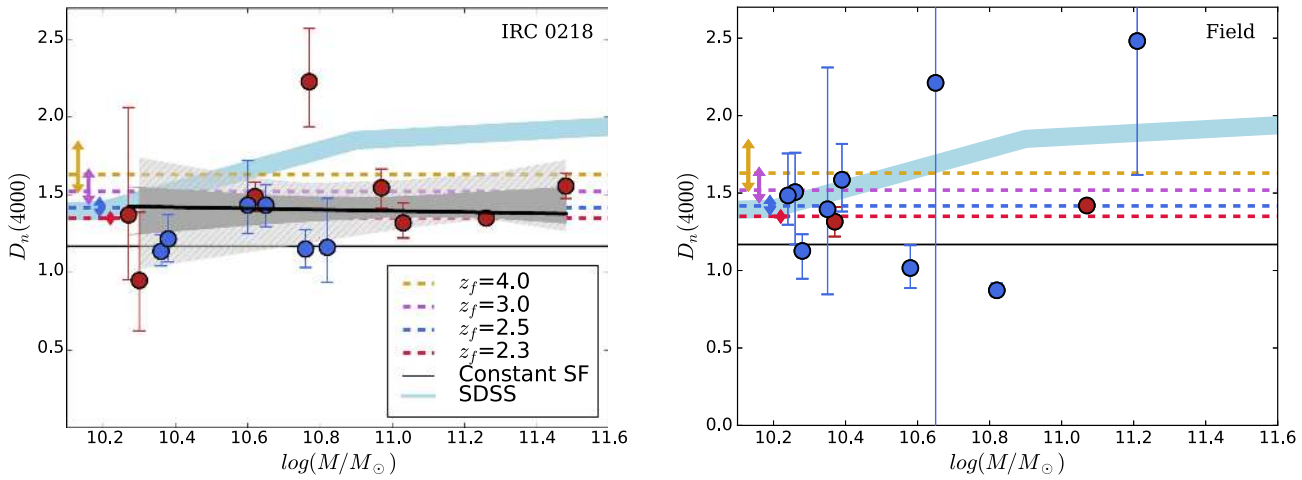

Figure 6. We plot $D_n(4000)$ against stellar mass for the protocluster (left) and field (right) G102 grism samples. Red and blue points represent quiescent and star-forming galaxies, respectively, as determined by galaxy *UVJ* colors (see Figure 4). The thick blue line shows the approximate mean $D_n(4000)$ from an analysis of SDSS data by Kauffmann et al. (2003). The successive horizontal lines show $D_n(4000)$ predicted by Bruzual & Charlot (2003) galaxy spectral evolution models with $Z = 0.02$ and exponentially declining star-formation histories ($\tau = 300$ Myr), for a variety of formation redshifts. Arrows attached to the exponential SFH lines indicate the change in $D_n(4000)$ produced by changing galaxy metallicity to $Z = 0.05$ or $Z = 0.004$. In the left-hand panel, we show a weighted linear regression fit to $D_n(4000)$ as a function of mass for the quiescent protocluster galaxies, as described in Section 4.2. The solid (hatched) shaded region around the fit shows the upper and lower 68% (95%) confidence interval on the fit. *Note:* one star-forming field galaxy from Table 3 (ID: 32468) has a negative $D_n(4000)$ due to poorly constrained redshift, and is omitted from the figure.

At masses below $M_* = 10^{10.85}\,M_\odot$, we find that the quiescent fraction in IRC 0218 is consistent with the field value at $z \sim 1.6$. This mirrors the trends observed in the clusters examined by Newman et al. (2014) and Cooke et al. (2016), and is consistent with the results of Nantais et al. (2016). Therefore, it appears that, if there is an environmental effect on the assembly of the red sequence at these redshifts, it is mass-dependent—primarily impacting high-mass galaxies with $M_* \geqslant 10^{10.85}\,M_\odot$, at least at $z > 1.5$.

To look for evidence of an evolution in f_Q at high redshifts, we compared our quiescent fraction results with those from the GEEC2 group and GCLASS cluster surveys at $z \sim 1$ (Balogh et al. 2016). We find no evidence that the quiescent fraction in dense environments at stellar masses ($M_* \geqslant 10^{10.85}\,M_\odot$) evolves as a function of redshift over $1 \leqslant z \leqslant 1.6$. as seen in Figure 7, at least for the clusters shown. This is at odds with the work by Nantais et al. (2017), where environmental quenching efficiency was shown to strongly evolve between $z = 1.6$ and $z = 0.9$. However, the apparent absence of evolution at high masses that we find would be consistent with the scenario discussed previously, in which the three high-redshift clusters given in Figure 5 were more evolved than the average $z \sim 1.6$ cluster (or conversely, that the SpARCS clusters (Nantais et al. 2017) were less-evolved than average). Observations of more high-z clusters are needed to better understand the high variation in cluster-to-cluster properties, and may help to resolve the relative evolutionary state of IRC 0218.

Drawing conclusions at lower halo masses is difficult, due to the uncertain masses of the high-redshift clusters and small number statistics, but IRC 0218 is likely a progenitor of a typical $M_* = 10^{14}$–$10^{14.5}\,M_\odot$ cluster at $z = 1$ (Rudnick et al. 2012), i.e., its likely descendant would be a GCLASS cluster, rather than a GEEC2 group. If this is so, then the end with lower stellar mass would appear to evolve in its quiescent fraction over $1 \leqslant z \leqslant 1.8$, increasing by a factor of $\sim$1.5$\times$ for galaxies of mass $10^{10.2}\,M_\odot \leqslant M_* \leqslant 10^{10.85}\,M_\odot$. The JKCS 041 sample does not extend to low enough masses to test this conclusion, but the $z = 1.5$ Cooke et al. (2016) cluster is consistent with our inference from IRC 0218.

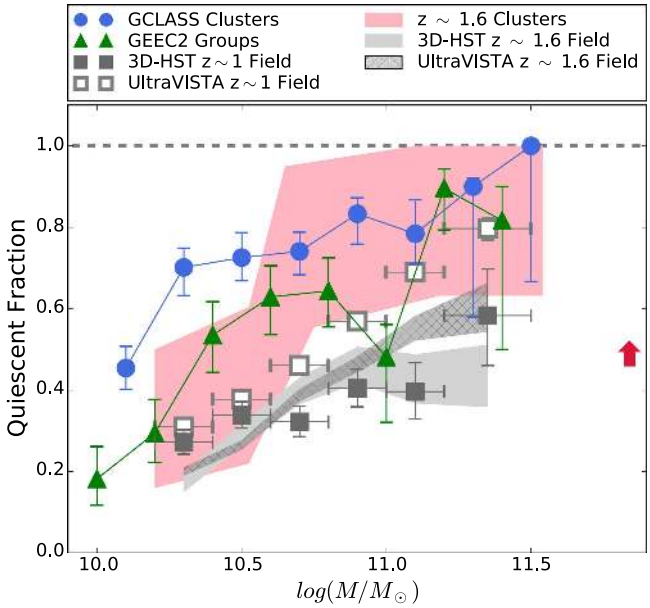

Figure 7. The quiescent fraction of galaxies as a function of stellar mass from the GEEC2 group and GCLASS cluster samples (Balogh et al. 2016) at $z \sim 1$. The field sample (solid gray squares) here consists of 3D-*HST* galaxies with masses $M_* \geqslant 10^{10.2}\,M_\odot$ and redshifts $0.9 \leqslant z \leqslant 1.1$. The solid background regions correspond to the envelopes traced out by the 68% binomial confidence limits for the higher-redshift dense environment (light red) and field (gray) samples from Figure 5. The hatched region corresponds to f_Q for UltraVISTA galaxies chosen using the *UVJ* criteria given in Muzzin et al. (2013a). The open points show f_Q for UltraVISTA galaxies chosen in the same way as the 3D-*HST* $z \sim 1$ field sample. We note that, for the field samples, the stellar masses plotted were chosen to be consistent with the $M_* = 10^{10.2}\,M_\odot$ IRC 0218 stellar mass limit. The red arrow indicates the approximate change in values of f_Q derived from 3D-*HST* galaxies if the *UVJ* criteria of Williams et al. (2009) were adopted.

Interpreting the behavior in the field over the same redshift range is more difficult. If we compare the 3D-*HST* $z \sim 1.6$ field sample detailed in Section 4.1 to a sample consisting of 3D-*HST* galaxies with redshifts $0.9 \lesssim z \lesssim 1.1$, we see no evidence for evolution in f_Q over the redshift range $1 \lesssim z \lesssim 1.6$ (see Figure 7). On the other hand, we can instead construct the $z \sim 1.6$ and $z \sim 1$ field samples using UltraVISTA galaxies from the version 4.1 catalog release (Muzzin et al. 2013a). For the UltraVISTA field sample, we adopt the slightly different, redshift-dependent *UVJ* criteria described in Muzzin et al. (2013a), in order to better separate the UltraVISTA red sequence galaxies (see below). At $z \sim 1.6$, we find that the UltraVISTA field is consistent with the 3D-*HST* field sample over our mass range, but at $z \sim 1$, the UltraVISTA f_Q values are systematically higher over all masses.

The largest contributor to the $z \sim 1$ discrepancy between 3D-*HST* and UltraVISTA appears to be a relatively large offset in rest-frame color between the two surveys. This offset between the two surveys is only apparent at $z = 1$, not at $z = 1.6$, which indicates a redshift-dependent difference in the rest-frame colors of the two surveys. Use of the Muzzin et al. (2013a) *UVJ* criteria to separate UltraVISTA galaxies somewhat lessens the differences in f_Q at $z \sim 1$, relative to using the Whitaker et al. (2012) criteria for both 3D-*HST* and UltraVISTA. However, as shown in Figure 7, the discrepancy is still significant—particularly at higher masses. We show the *UVJ* diagrams for 3D-*HST* and UltraVISTA, the different *UVJ* selection criteria, and the differences in rest-frame color between the two surveys in Appendix A, and note that this situation illustrates that extreme caution must be exercised when comparing f_Q between different surveys.

Ultimately, we refrain from drawing any firm conclusions about f_Q evolution in the field, due to the discrepancy between the 3D-*HST* and UltraVISTA field galaxy quiescent fractions. However, at low masses, both the 3D-*HST* and UltraVISTA field $z \sim 1$ f_Q values are elevated relative to the $z = 1.6$ values. If we were to take this mild quiescent fraction evolution in low stellar mass field galaxies at face value, it would contrast with the significant evolution seen in the clusters at low stellar masses over the same redshift range. This could imply that the cluster is more effective at quenching low-mass galaxies than processes at play in the field (e.g., Tomczak et al. 2014). More cluster studies and careful treatment of *UVJ* selection effects are needed to evaluate this possibility.

5.2. $D_n(4000)$ and Stellar Mass

If the same SFH is assumed for all galaxies, a lack of $D_n(4000)$ dependence with stellar mass implies no age trend along the red sequence. An absence of such a trend could be explained by dry (gasless) merging, which would serve to redistribute stellar mass on the red sequence; this would scramble any trend in age, and thus $D_n(4000)$, with stellar mass. The evolutionary state of IRC 0218 implies a high merger rate, and evidence for an elevated rate has been found by previous studies (Papovich et al. 2012; Rudnick et al. 2012; Lotz et al. 2013). Lotz et al. (2013) found that most of the mergers were between passive galaxies, consistent with them being mostly dry (gasless) and therefore not hosting any new star formation. However, future work is needed to investigate the possible impacts of dry merging on red sequence $D_n(4000)$ through measurements of galaxy morphology and $D_n(4000)$ in more high-redshift clusters.

On the other hand, if merging is not important, then the mass dependence of f_Q, coupled with a lack of similar trend in $D_n(4000)$, indicates that the quenching of star formation may have happened at roughly the same epoch, in such a way as to imprint the f_Q–M_* trend. Our data are too limited to highly constrain such a scenario, but speculatively, such a quenching episode could be associated with the initial formation of the protocluster core, as our G102 data only span the densest region of IRC 0218. Clearly, more $D_n(4000)$ measurements in high-redshift clusters are needed to distinguish the various processes playing a role in these environments.

There is also the possibility that a true trend with stellar mass exists, as we are unable to rule out strong trends with slopes $\Delta D_n(4000) = +0.25 \log (M_\odot)^{-1}$ to $\Delta D_n(4000) = -0.2 \log (M_\odot)^{-1}$ over our mass range. Indeed, there is a common expectation that more massive cluster galaxies should have, on average, older populations (e.g., Rosati et al. 2009; Jørgensen and Chiboucas 2013; Tanaka et al. 2013). It may be that the relatively large uncertainties associated with our relation between $D_n(4000)$ and stellar mass (see Section 4.2) mask an underlying trend, or that $D_n(4000)$ is not sufficiently sensitive to age to reveal any trends in the IRC 0218 galaxies.

We do note that the weighted mean $D_n(4000)$ for the red sequence galaxies in the protocluster is the same as the value found in our field sample. With the caveat that our field sample only contains two quiescent galaxies, this result implies that the field and cluster galaxies we examined did not quench at appreciably different times, although the cluster environment apparently quenched more efficiently at a given stellar mass, at least for masses $M_* \geqslant 10^{10.85} M_\odot$. Simulations predict such "accelerated evolution" of cluster environments due to earlier collapse of dark matter halos (De Lucia et al. 2004). This is supported by more recent observations of both IRC 0218 (Papovich et al. 2012) and other environments (Strazzullo et al. 2013; Newman et al. 2014). Under such a scenario—even if higher-mass galaxies in dense environments quench earlier than lower-mass galaxies—if evolution and/or quenching in dense environments is accelerated, then the age differences between galaxies may be too small to show statistically significant trend in $D_n(4000)$, given the uncertainties in our slope described previously. Demonstration of a strong $D_n(4000)$–M_* relation in high-redshift clusters could place constraints on any potential accelerated evolution in dense environments.

Under assumptions regarding SFH, we can translate between $D_n(4000)$ and stellar age/formation redshift. In this work, we adopt a common, exponentially declining SFH with characteristic timescale $\tau = 300$ Myr and metallicity $Z = 0.02$. Using GALAXEV (Bruzual & Charlot 2003) to model galaxy spectral evolution under this SFH, we show the predicted $D_n(4000)$ values for various formation redshifts in Figure 6. We find that the quiescent galaxies in IRC 0218 are largely consistent with star formation starting in the redshift range $2.3 \lesssim z_f \lesssim 3$, consistent with the formation epoch estimated by Papovich et al. (2010) on the basis of $(U - B)$ colors, and similar to the z_f estimated by several other high-redshift cluster studies, as well as studies of $z < 1$ environments (e.g., Bower et al. 1998; Poggianti et al. 2001; van Dokkum & van der Marel 2007; Hilton et al. 2009; Mei et al. 2009).

Several galaxies are consistent with very high formation redshifts, $z_f \gtrsim 4$; these high z_f values are consistent with the $z \sim 1$ observations by Muzzin et al. (2012), who found

quiescent galaxies in clusters with ages approaching the age of the universe. Such high z_f values place strong constraints on possible quenching mechanisms; any possible mechanism would need to be capable of truncating star formation in the limited time before $z \sim 3$. For example, a galaxy that formed stars until $z = 4$, and was subsequently quenched by $z = 3$, would have had the quenching occur over a period of only ~600 Myr. This limited time interval naturally disfavors known low-redshift quenching mechanisms operating on long timescales (e.g., delayed quenching or strangulation, Wetzel et al. 2013; Peng et al. 2015), and favors more abrupt mechanisms (e.g., luminous AGN feedback, Bongiorno et al. 2016), in line with several other high-redshift cluster studies (Brodwin et al. 2013; Alberts et al. 2016).

Our results regarding z_f are highly dependent on adopted SFH. If a common $\tau = 300$ Myr, $Z = 0.02$ SFH is appropriate, then we can rule out red sequence formation ages more recent than $z = 2.3$, as those galaxies would not meet our *UVJ* cut (see Figure 4). However, if instead we adopted a single stellar population with the same metallicity, then we could not rule out formation redshifts as recent as $z \leqslant 2$.

The effects of raising or lowering adopted galaxy metallicity are illustrated in Figure 6. As can be seen, changing galaxy metallicity would impact our z_f results; $D_n(4000)$ is relatively sensitive to metallicity, with higher metallicities leading to higher $D_n(4000)$ for a given stellar age. Full spectral fitting may alleviate some of the sensitivity to metallicity.

On the other hand, if metallicity were somehow masking a positive correlation between $D_n(4000)$ and stellar mass, then metallicity would need to be negatively correlated with stellar mass. Such an inverse relation is not observed in studies at both low and high redshifts (see Tremonti et al. 2004 and Gallazzi et al. 2005, for low redshift; Erb et al. 2006, Zahid et al. 2014, and Tran et al. 2015 study high redshift). Therefore, metallicity effects are likely not responsible for the flat $D_n(4000)$–M_* relation we observe.

6. Conclusion

We present the results of a study of 14 quiescent and star-forming galaxies in the largest subgroup of the $z = 1.62$ protocluster IRC 0218, down to stellar masses $M_* = 10^{10.2}\,M_\odot$. Using IR photometry, *Hubble*/WFC3 grism spectroscopy of the rest-frame 4000 Å break, and a mixture of spectroscopic and grism redshifts, we classified galaxies in the protocluster and field as star-forming or quiescent, based on their rest-frame $(U - V)$ and $(V - J)$ colors. Stellar masses were estimated through template fitting, and the spectroscopic index $D_n(4000)$ was measured for each galaxy.

Considering protocluster galaxies with $M_* \geqslant 10^{10.85}\,M_\odot$, we find the quiescent fraction in IRC 0218 to be $f_Q = 1.0^{+0.00}_{-0.37}$. This value is two times higher than the value in the field, which we find to be $f_Q = 0.45^{+0.03}_{-0.03}$, albeit there are only four galaxies in our protocluster sample with masses $M_* \geqslant 10^{10.85}\,M_\odot$. At lower masses, $10^{10.2}\,M_\odot \leqslant M_* \leqslant 10^{10.85}\,M_\odot$, the protocluster and field have consistent f_Q, with $f_Q = 0.40^{+0.20}_{-0.18}$ in the cluster and $f_Q = 0.28^{+0.02}_{-0.02}$ in the field.

Although our conclusion of an elevated f_Q at high masses in IRC 0218 is of marginal significance due to our small sample size, it is consistent with two other high-redshift cluster studies. However, we do note that there are other, similar-redshift clusters in the literature with high-mass quiescent fractions that are consistent with values in the field, though the clusters are all consistent within their formal uncertainties. It is therefore difficult to determine if the range in quiescent fractions reflects a true cluster-to-cluster variation or is dominated by statistical uncertainties.

Comparing our results and those from two other protoclusters with studies of groups and clusters at $z \sim 1$, we see no evolution in the quiescent fraction at masses $M_* \geqslant 10^{10.85}\,M_\odot$ between $z \sim 1.6$ and $z \sim 1$. On the other hand, there is one recently published sample of clusters at $z \sim 1.6$ that does show significant evolution to $z \sim 1$, again implying a large cluster-to-cluster variation in properties. For the end with low stellar mass, $10^{10.2}\,M_\odot \leqslant M_* \leqslant 10^{10.85}\,M_\odot$, comparing IRC 0218 with likely descendants at $z \sim 1$ indicates that f_Q may increase modestly between the two epochs.

Our data are consistent with the null hypothesis of no trend between $D_n(4000)$ and stellar mass for quiescent protocluster galaxies above our mass limit. However, the data are also consistent at the $<2\sigma$ level with significant trends of $D_n(4000)$ with stellar mass. The null hypothesis is consistent with a scenario in which the high merger rate in IRC 0218 has redistributed red sequence mass, masking any previously existing trend in $D_n(4000)$. Alternately, it may suggest that the trend in f_Q was imprinted as the protocluster red sequence galaxies quenched over a short period of time. Overall, we find that, as expected, quiescent galaxies in the cluster and field have elevated $D_n(4000)$, relative to star-forming galaxies.

Under an adopted $\tau = 300$ Myr, $Z = 0.02$ exponentially declining SFH, we can rule out quiescent galaxies forming more recently than $z = 2.3$. Most quiescent galaxies in the cluster formed in the redshift range $2.3 \lesssim z_f \lesssim 3$. Several red sequence galaxies have very high formation redshifts, consistent with $z_f \gtrsim 4$, placing strong timescale constraints on any potential quenching mechanism.

This work is based on observations taken with the NASA/ESA *HST* as part of the 3D-*HST* Treasury Program (GO 12177 and 12328), which is operated by the Association of Universities for Research in Astronomy, Inc., under NASA contract NAS5-26555. This work is also based on NASA/ESA *HST* observations taken as part of program GO 12590, supported by NASA through a grant from the Space Telescope Science Institute. D.L.B. gratefully acknowledges support from NSF grant AST-1211621. G.R. acknowledges the support of NASA grant HST-GO-12590.011-A, NSF grants 1211358 and 1517815, the support of an ESO visiting fellowship, and the hospitality of the Max Planck Institute for Extraterrestrial Physics, as well as Hamburg Observatory. K. Tran acknowledges support by the National Science Foundation under grant number 1410728. C.N.A.W. acknowledges the support of NASA grant HST-GO-12590.09-A. D.L.B. and G.R. thank Katherine Whitaker and Adam Muzzin for helpful discussion. The authors thank the anonymous referee for constructive comments.

Appendix A
The 3D-*HST* and UltraVISTA *UVJ* Selection Criteria

In Figure 8, we show the rest-frame *UVJ* colors for the UltraVISTA and 3D-*HST* $z \sim 1.6$ and $z \sim 1$ field samples. It is apparent that an offset in rest-frame color exists between the two surveys at $z \sim 1$, but not at $z \sim 1.6$. The result of this redshift-dependent offset is that the 3D-*HST UVJ* criteria (black lines in Figure 8) used by Whitaker et al. (2012) adequately

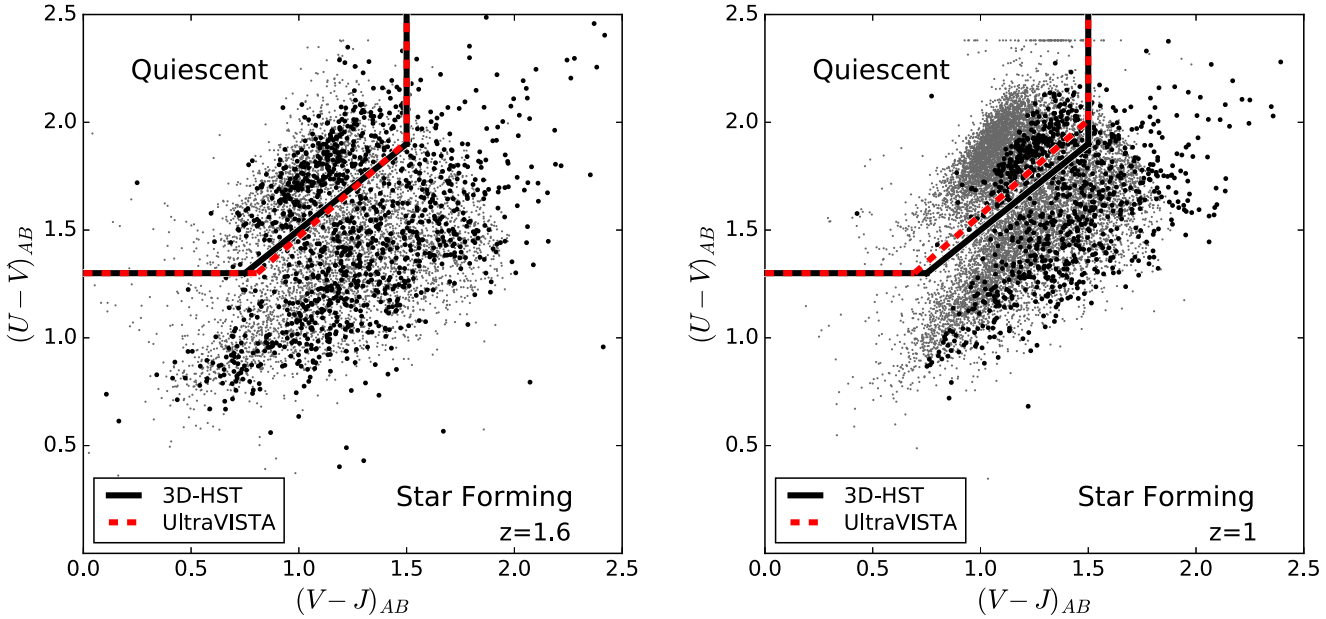

Figure 8. Rest-frame *UVJ* colors for $z \sim 1.6$ (left panel) and $z \sim 1$ (right) galaxies in UltraVISTA (gray background points) and 3D-*HST* (black foreground points). The black solid lines give the *UVJ* selection criteria for 3D-*HST* galaxies as defined in Whitaker et al. (2012). The dashed red lines show the redshift-dependent criteria adopted by Muzzin et al. (2013a) for UltraVISTA galaxies.

separate the red sequence galaxies in the 3D-*HST* data, but overlap with the star-forming sequence of galaxies in the UltraVISTA catalog. This, in turn, results in a higher f_Q for the UltraVISTA sample at $z \sim 1$, relative to 3D-*HST*. Thus, for the UltraVISTA galaxies, we instead adopt the slightly different $z \leqslant 1$ and $z \geqslant 1$ *UVJ* criteria given in Muzzin et al. (2013a) (red dashed lines in Figure 8). These criteria better trace the gap between the red sequence and star-forming galaxies in UltraVISTA at $z \sim 1$, and are nearly identical to the Whitaker et al. (2012) criteria at $z \sim 1.6$. However, based on the positions of the two sets of *UVJ* lines in Figure 8, it appears that, even after these changes, UltraVISTA and 3D-*HST* galaxies are not being separated into quiescent and star-forming populations in the same way at $z \sim 1$. This difference may be driving the systematic offset in f_Q we observe between the two surveys at $z \sim 1$ (see Section 5).

References

Alberts, S., Pope, A., Brodwin, M., et al. 2016, ApJ, 825, 72
Andreon, S., Maughan, B., Trinchieri, G., & Kurk, J. 2009, A&A, 507, 147
Balogh, M., Eke, V., Miller, C., et al. 2004, MNRAS, 348, 1355
Balogh, M. L., McGee, S. L., Mok, A., et al. 2016, MNRAS, 456, 4364
Balogh, M. L., Morris, S. L., Yee, H. K. C., Carlberg, R. G., & Ellingson, E. 1999, ApJ, 527, 54
Bassett, R., Papovich, C., Lotz, J. M., et al. 2013, ApJ, 770, 58
Bongiorno, A., Schulze, A., Merloni, A., et al. 2016, A&A, 588, A78
Bower, R. G., Kodama, T., & Terlevich, A. 1998, MNRAS, 299, 1193
Brammer, G. B., van Dokkum, P. G., Franx, M., et al. 2012, ApJS, 200, 13
Brodwin, M., McDonald, M., Gonzalez, A. H., et al. 2016, ApJ, 817, 122
Brodwin, M., Stanford, S. A., Gonzalez, A. H., et al. 2013, ApJ, 779, 138
Bruzual, A. G. 1983, ApJ, 273, 105
Bruzual, G., & Charlot, S. 2003, MNRAS, 344, 1000
Butcher, H., & Oemler, A., Jr. 1978, ApJ, 219, 18
Calzetti, D., Armus, L., Bohlin, R. C., et al. 2000, ApJ, 533, 682
Chabrier, G. 2003, PASP, 115, 763
Chung, S. M., Eisenhardt, P. R., Gonzalez, A. H., et al. 2011, ApJ, 743, 34
Cooke, E. A., Hatch, N. A., Stern, D., et al. 2016, ApJ, 816, 83
Croton, D. J., Springel, V., White, S. D. M., et al. 2006, MNRAS, 365, 11
Delaye, L., Huertas-Company, M., Mei, S., et al. 2014, MNRAS, 441, 203
De Lucia, G., Kauffmann, G., & White, S. D. M. 2004, MNRAS, 349, 1101
Erb, D. K., Shapley, A. E., Pettini, M., et al. 2006, ApJ, 644, 813
Fassbender, R., Nastasi, A., Santos, J. S., et al. 2014, A&A, 568, A5
Finoguenov, A., Watson, M. G., Tanaka, M., et al. 2010, MNRAS, 403, 2063
Gallazzi, A., Charlot, S., Brinchmann, J., White, S. D. M., & Tremonti, C. A. 2005, MNRAS, 362, 41
Gehrels, N. 1986, ApJ, 303, 336
Gobat, R., Daddi, E., Onodera, M., et al. 2011, A&A, 526, A133
Gómez, P. L., Nichol, R. C., Miller, C. J., et al. 2003, ApJ, 584, 210
Grogin, N. A., Kocevski, D. D., Faber, S. M., et al. 2011, ApJS, 197, 35
Gunn, J. E., & Gott, J. R., III 1972, ApJ, 176, 1
Hashimoto, Y., Oemler, A., Jr., Lin, H., & Tucker, D. L. 1998, ApJ, 499, 589
Hatch, N. A., Muldrew, S. I., Cooke, E. A., et al. 2016, MNRAS, 459, 387
Henke, B. 2015, Master's thesis, The Univ. Kansas
Hilton, M., Stanford, S. A., Stott, J. P., et al. 2009, ApJ, 697, 436
Hogg, D. W., Blanton, M. R., Brinchmann, J., et al. 2004, ApJL, 601, L29
Horne, K. 1986, PASP, 98, 609
Jørgensen, I., & Chiboucas, K. 2013, AJ, 145, 77
Kauffmann, G., Heckman, T. M., White, S. D. M., et al. 2003, MNRAS, 341, 54
Koekemoer, A. M., Faber, S. M., Ferguson, H. C., et al. 2011, ApJS, 197, 36
Kriek, M., van der Wel, A., van Dokkum, P. G., Franx, M., & Illingworth, G. D. 2008, ApJ, 682, 896
Kriek, M., van Dokkum, P. G., Labbé, I., et al. 2009, ApJ, 700, 221
Larson, R. B., Tinsley, B. M., & Caldwell, C. N. 1980, ApJ, 237, 692
Lawrence, A., Warren, S. J., Almaini, O., et al. 2007, MNRAS, 379, 1599
Lee, S.-K., Im, M., Kim, J.-W., et al. 2015, ApJ, 810, 90
Lewis, I., Balogh, M., De Propris, R., et al. 2002, MNRAS, 334, 673
Lotz, J. M., Papovich, C., Faber, S. M., et al. 2013, ApJ, 773, 154
Marchesini, D., van Dokkum, P. G., Förster Schreiber, N. M., et al. 2009, ApJ, 701, 1765
Mei, S., Holden, B. P., Blakeslee, J. P., et al. 2009, ApJ, 690, 42
Mei, S., Scarlata, C., Pentericci, L., et al. 2015, ApJ, 804, 117
Momcheva, I. G., Brammer, G. B., van Dokkum, P. G., et al. 2016, ApJS, 225, 27
Muzzin, A., Marchesini, D., Stefanon, M., et al. 2013a, ApJ, 777, 18
Muzzin, A., Wilson, G., Demarco, R., et al. 2013b, ApJ, 767, 39
Muzzin, A., Wilson, G., Yee, H. K. C., et al. 2012, ApJ, 746, 188
Nantais, J. B., Muzzin, A., van der Burg, R. F. J., et al. 2017, MNRAS, 465, L104
Nantais, J. B., van der Burg, R. F. J., Lidman, C., et al. 2016, A&A, 592, A161
Newman, A. B., Ellis, R. S., Andreon, S., et al. 2014, ApJ, 788, 51
Papovich, C., Bassett, R., Lotz, J. M., et al. 2012, ApJ, 750, 93
Papovich, C., Momcheva, I., Willmer, C. N. A., et al. 2010, ApJ, 716, 1503
Patel, S. G., Holden, B. P., Kelson, D. D., Illingworth, G. D., & Franx, M. 2009, ApJL, 705, L67

Peng, Y., Maiolino, R., & Cochrane, R. 2015, Natur, 521, 192
Peng, Y.-j., Lilly, S. J., Kovač, K., et al. 2010, ApJ, 721, 193
Phillips, J. I., Wheeler, C., Boylan-Kolchin, M., et al. 2014, MNRAS, 437, 1930
Pierre, M., Clerc, N., Maughan, B., et al. 2012, A&A, 540, A4
Poggianti, B. M., Bridges, T. J., Carter, D., et al. 2001, ApJ, 563, 118
Quadri, R. F., Williams, R. J., Franx, M., & Hildebrandt, H. 2012, ApJ, 744, 88
Rosati, P., Tozzi, P., Gobat, R., et al. 2009, A&A, 508, 583
Rudnick, G., Rix, H.-W., & Kennicutt, R. C., Jr. 2000, ApJ, 538, 569
Rudnick, G. H., Tran, K.-V., Papovich, C., Momcheva, I., & Willmer, C. 2012, ApJ, 755, 14
Santos, J. S., Fassbender, R., Nastasi, A., et al. 2011, A&A, 531, L15
Skelton, R. E., Whitaker, K. E., Momcheva, I. G., et al. 2014, ApJS, 214, 24
Stanford, S. A., Brodwin, M., Gonzalez, A. H., et al. 2012, ApJ, 753, 164
Straatman, C. M. S., Labbé, I., Spitler, L. R., et al. 2014, ApJL, 783, L14
Strazzullo, V., Gobat, R., Daddi, E., et al. 2013, ApJ, 772, 118
Tadaki, K.-i., Kodama, T., Ota, K., et al. 2012, MNRAS, 423, 2617
Tal, T., Dekel, A., Oesch, P., et al. 2014, ApJ, 789, 164
Tanaka, M., Finoguenov, A., & Ueda, Y. 2010, ApJL, 716, L152
Tanaka, M., Toft, S., Marchesini, D., et al. 2013, ApJ, 772, 113
Tomczak, A. R., Quadri, R. F., Tran, K.-V. H., et al. 2014, ApJ, 783, 85
Tran, K.-V. H., Nanayakkara, T., Yuan, T., et al. 2015, ApJ, 811, 28
Tremonti, C. A., Heckman, T. M., Kauffmann, G., et al. 2004, ApJ, 613, 898
van den Bosch, F. C., Aquino, D., Yang, X., et al. 2008, MNRAS, 387, 79
van Dokkum, P. G., & van der Marel, R. P. 2007, ApJ, 655, 30
Wang, T., Elbaz, D., Daddi, E., et al. 2016, ApJ, 828, 56
Webb, T., Noble, A., DeGroot, A., et al. 2015, ApJ, 809, 173
Wetzel, A. R., Tinker, J. L., Conroy, C., & van den Bosch, F. C. 2013, MNRAS, 432, 336
Whitaker, K. E., van Dokkum, P. G., Brammer, G., et al. 2013, ApJL, 770, L39
Whitaker, K. E., van Dokkum, P. G., Brammer, G., & Franx, M. 2012, ApJL, 754, L29
Williams, R. J., Quadri, R. F., Franx, M., van Dokkum, P., & Labbé, I. 2009, ApJ, 691, 1879
Wong, K. C., Tran, K.-V. H., Suyu, S. H., et al. 2014, ApJL, 789, L31
Wuyts, S., Labbé, I., Franx, M., et al. 2007, ApJ, 655, 51
Zahid, H. J., Kashino, D., Silverman, J. D., et al. 2014, ApJ, 792, 75
Zeimann, G. R., Stanford, S. A., Brodwin, M., et al. 2012, ApJ, 756, 115